



TiO₂–RuO₂ electrocatalyst supports exhibit exceptional electrochemical stability

Chih-Ping Lo, Guanxiong Wang, Amod Kumar, Vijay Ramani*

Center for Electrochemical Science and Engineering, Department of Chemical & Biological Engineering, 10 W 33rd Street, 127 Perlstein Hall, Illinois Institute of Technology, Chicago, IL 60616, USA

ARTICLE INFO

Article history:

Received 6 September 2012

Received in revised form 2 March 2013

Accepted 25 March 2013

Available online 3 April 2013

Keywords:

Electrocatalyst support

Polymer electrolyte fuel cell

Carbon corrosion

Mixed metal oxides

ABSTRACT

Titanium dioxide–ruthenium dioxide (TiO₂–RuO₂; TRO) powders were prepared in both the hydrous and anhydrous form using a wet chemical synthesis procedure. These materials were characterized by XRD, TEM, and BET. Their electrical conductivity and electrochemical properties such as stability under potential cycling, electrochemical surface area (ECSA), electrocatalytic activity, and fuel cell performance were measured. Anhydrous TiO₂–RuO₂ (TRO-a) demonstrated exceptional electrochemical stability compared to baseline Vulcan XC-72R carbon when tested using an aggressive accelerated stability test (AST) protocol. The various TRO powders were catalyzed by depositing platinum nanoparticles by an impregnation–reduction method to yield Pt/TRO electrocatalysts. The Pt/TRO-a electrocatalysts had a mass activity of 54 mA mg_{Pt}^{−1} and a specific activity of 284 μA cm_{Pt}^{−2} for the oxygen reduction reaction. Fuel cell polarization data was obtained on membrane electrode assemblies (MEAs) prepared with Pt/TRO and baseline Pt/C electrocatalysts showed that the Pt-TRO-based MEAs exhibited very good performance. The performance obtained was below the Pt/C benchmark, however, further improvements in performance are expected with greater optimization of the Pt particle size and electrode structure.

© 2013 Elsevier B.V. All rights reserved.

1. Introduction

Polymer electrolyte fuel cells (PEFCs) have the potential to serve as efficient, environment friendly and modular electrochemical energy conversion devices with applications in the automotive, stationary power, and portable/military sectors. Over the past several years, much research has been focused on improving the performance of PEFCs and their constituent components [1–4]. One of the key remaining challenges is the enhancement of PEFC component durability and reliability [5]. Presently, the most widely used electrocatalyst in PEFCs membrane electrode assemblies (MEAs) is platinum supported on high surface area carbon [6]. However, the carbon support has limitations in terms of its electrochemical stability. Electrooxidation of the carbon support (i.e., carbon corrosion) can occur during fuel cell operation. The reaction rate for the electrooxidation of carbon can increase dramatically under certain transient operating conditions (e.g., PEFC start-up/shut-down; fuel starvation) [7]. The local electrode potential at the cathode and/or the anode can escalate up to 2 V under these conditions, resulting in an extremely large overpotential (and hence reaction rate) for the carbon electrooxidation reaction [8]. The consequent irreversible loss of carbon causes the release of attached platinum

particles. These particles become electrically isolated, leading to lower Pt utilization as well as a marked degradation in fuel cell performance [9,10]. Carbon corrosion also causes the agglomeration and sintering of Pt particles, leading to a loss in the electrochemically active surface area (ECSA) of the PEFC electrode [11]. To address the issue of catalyst support corrosion, much effort has been devoted to developing more stable carbon materials, some with higher graphitic character, such as carbon nanotubes [12,13], nanocoils [14,15], nanohorns [16], nanofibers [17,18] and graphene [19]. However, most of these carbon materials are still susceptible to corrosion at high electrode (over)potentials [20]. Various alternative non-carbon catalyst support materials have been investigated, including SnO₂ [21,22], ITO [23], WO_x [24,25], TiO₂ [26,27], RuO₂ [28,29], SiO₂ [30,31], and WC [32,33]. Some of the metal oxide supports have been shown to act as a co-catalyst and thereby enhance the activity of the supported electrocatalyst [34–38].

For example, RuO₂–TiO₂ has been used as a candidate material for dimensionally stable anodes [39,40]. This material was found to demonstrate high electrical conductivity and also demonstrated high chemical stability in acidic and oxidative environments [39,40]. Recently, RuO₂–TiO₂ binary oxides have also been used as a catalyst support for fuel cell applications. Haas et al. [26] reported that Pt/Ru_xTi_{1−x}O₂ catalysts had an ECSA, as measured by cyclic voltammetry in a half-cell configuration, comparable to that of commercial carbon supported catalysts. However, no stability and fuel cell performance testing of these materials was

* Corresponding author. Tel.: +1 312 567 3064; fax: +1 312 567 8874.

E-mail addresses: ramani@iit.edu, akumar18@hawk.iit.edu (V. Ramani).

conducted/reported by the authors. Huang et al. demonstrated that TiO_2 , when used as a catalyst support, exhibited excellent stability and fuel cell performance [41]. The ECSA of the Pt/ TiO_2 electrocatalyst decreased by only about 20% after the potential was held at 1.2 V for 80 h, as compared with a 93% loss in ECSA in a baseline Pt/C catalyst after a similar test. However, the stability and conductivity of the stand-alone support was not reported. The use of hydrous RuO_2 as an electrocatalyst support in fuel cells has also received attention due to its mixed-conducting properties [42]. Prior research has shown that Pt/ $\text{RuO}_2 \cdot x\text{H}_2\text{O}$ possesses higher electrocatalytic activity toward methanol oxidation compared with PtRu black [29]. More recently, Ho et al. [43] synthesized $\text{Ti}_{0.7}\text{Ru}_{0.3}\text{O}_2$ as a co-catalyst support for Pt. The $\text{Ti}_{0.7}\text{Ru}_{0.3}\text{O}_2$ support was shown to induce electronic interactions with the metal particles, leading to an enhancement of CO-tolerance, catalytic activity, and durability due to both the strong metal-support interactions and the high proton conductivity of hydrated $\text{Ti}_{0.7}\text{Ru}_{0.3}\text{O}_2$. Both direct methanol fuel cells (DMFCs) and PEFCs with Pt/ $\text{Ti}_{0.7}\text{Ru}_{0.3}\text{O}_2$ catalyst as anodes demonstrated better performance than their counterparts with a baseline Pt/C catalyst. This study did not report any stability data or use of these catalysts at the cathode, which is the electrode experiencing excursions to high potentials during fuel cell operation.

Carbon corrosion can occur at both the anode and cathode during fuel cell start-up/shut-down and under fuel starvation conditions [7]. Merely studying the change in ECSA of a catalyzed support does not in itself provide any indication of stand-alone support stability. Therefore, in this work, the stability of the catalyst supports was evaluated independently from that of the supported electrocatalyst. Moreover, the MEAs prepared in this study used Pt/ TiO_2 – RuO_2 catalyst at both the cathode and the anode. The possibility of enhancing the performance of the PEFC by utilizing hydrous RuO_2 catalyst supports that conduct both protons and electrons on their surface was also evaluated.

In this study, TiO_2 , a semiconductor known to be corrosion resistant in acidic and oxidative environments [27,41], was synthesized with high BET surface areas and tailored porosities. The role of TiO_2 in this study was to serve as a corrosion resistant, high surface area template for the final electrocatalyst support. Titanium dioxide–ruthenium dioxide powders in hydrous (TRO-h) and anhydrous (TRO-a) forms were prepared using a wet chemical synthesis procedure. The physical and electrochemical properties of this non-carbon support were systematically measured in both non-catalyzed and catalyzed forms.

2. Experimental

2.1. Reagents

The following chemicals were used as received: titanium(IV) oxide (TiO_2 , Aeroxide P25, Acros Organics), ruthenium(III) chloride hydrate ($\text{RuCl}_3 \cdot x\text{H}_2\text{O}$, 35–40% Ru, Acros Organics), chloroplatinic acid hexahydrate ($\text{H}_2\text{PtCl}_6 \cdot 6\text{H}_2\text{O}$, ACS reagent, $\geq 37.50\%$ Pt basis, Sigma–Aldrich), formic acid (HCOOH , $\sim 98\%$, Fluka), sodium hydroxide (NaOH , ACS, Fisher), hydrogen peroxide (H_2O_2 , 35 wt% solution in water, Acros Organics), 5 wt% Nafion® (1100 EW) (Solution Technologies, Mendenhall, PA). All aqueous solutions were prepared with 18.2 M Ω deionized water from a Millipore water system.

2.2. Preparation of TiO_2 – RuO_2

TiO_2 – RuO_2 powders were prepared by a simple wet chemical procedure [44]. In a typical synthesis, 12.5 mmol TiO_2 was dispersed in 250 mL DI water and sonicated for 30 min. 12.5 mmol

$\text{RuCl}_3 \cdot x\text{H}_2\text{O}$ was added into the mixture under stirring for 30 min. 0.05 N KOH(aq) was then dropped into the mixture under stirring until the pH of the solution reached 7. The black powder obtained was filtered out and washed repeatedly with deionized water. The powders were then dried at 120 °C for 8 h to yield hydrous TiO_2 – RuO_2 (TRO-h). A portion of the TRO-h was further calcined at 450 °C for 3 h in air to yield anhydrous TiO_2 – RuO_2 (TRO-a).

2.3. Preparation of 40 wt% Pt/ TiO_2 – RuO_2 electrocatalysts

Platinum nanoparticles were synthesized by the chemical reduction of Pt precursor with formic acid [45]. In a typical synthesis, a suspension of 5 mmol TRO-a or TRO-h support in reaction solution (1.9 mmol $\text{H}_2\text{PtCl}_6 \cdot 6\text{H}_2\text{O}$ and 30 mL HCOOH in 600 mL of water) was sonicated for 30 min. The suspension was heated at 80 °C for 2 h under vigorous stirring. The product obtained was collected by vacuum filtration and washed several times with deionized water, and then dried in an oven at 60 °C. For selected samples, additional heat treatment was conducted at 200 °C and 450 °C. The catalyst obtained was denoted as Pt/TRO-a-*b*, where *b* represented the annealing temperature to which the catalyst was exposed.

2.4. Characterization techniques

X-ray diffraction (XRD) was performed using a Rigaku Miniflex diffractometer to confirm the presence of ruthenium oxide and platinum and to estimate platinum crystallite size. Diffractograms were recorded in the range $2\theta = 20$ – 80° with a step of 2 min/degree.

Transmission electron microscopy (TEM) was used to determine the size and distribution of the platinum particles and support aggregates. TEM micrographs were obtained using a Jeol 2100F microscope equipped with a liquid nitrogen Si (Li) EDX detector, at an acceleration voltage of 200 kV.

A Brunauer–Emmett–Teller (BET) surface area analyzer was used to calculate the BET specific surface area by a multipoint analysis of nitrogen desorption isotherms.

The two-point probe technique was used in conjunction with linear-sweep voltammetry to measure the electrical conductivity of the supports. All experiments were conducted at room temperature and were performed on pellet samples using a Gamry potentiostat. Sample preparation and other experimental details are provided in the corresponding supporting information section.

2.5. Evaluation of electrochemical surface area (ECSA)

Electrochemical characterization was performed in a three-compartment electrochemical cell containing 0.1 M HClO_4 as the electrolyte. A glassy carbon disk (0.196 cm²) was used as the platform upon which the active material was deposited to yield the working electrode; a saturated calomel electrode (SCE) was used as the reference electrode; a Pt foil was used as the counter electrode. Details about ink and electrode preparation are provided under supporting information.

The electrolyte was purged with nitrogen gas for 30 min before the measurement. Due to minor contamination from the binder, the electrode potential was cycled 20 times at a scan rate of 100 mV/s between 0.05 and 1.2 V (vs. NHE) to produce a clean surface. Subsequently, a cyclic voltammogram (CV) was measured by scanning the working electrode potential between 0.05 and 1.2 V at a scan rate of 20 mV/s.

The ECSA was calculated by measuring the charge associated with hydrogen desorption (*C*) between 0.05 and 0.4 V and assuming 210 $\mu\text{C cm}^{-2}$ as the conversion factor corresponding to the charge associated with the adsorption of one monolayer of hydrogen on

the surface of polycrystalline platinum [46]. The ECSA of Pt was calculated based on the relation

$$\text{ECSA} = \left[\frac{C}{210L_{\text{Pt}} \times A_{\text{g}}} \right] 10^5 \quad (1)$$

where L_{Pt} is the loading of Pt ($\text{mg}_{\text{Pt}} \text{ cm}^{-2}$) on the working electrode and A_{g} (cm^2) is the geometric area of the working electrode.

2.6. Evaluation of stability using accelerated stability test (AST) protocols

The AST protocols (start-stop and load cycling protocols) [47] employed in this study are as follows: for evaluating the stability of the support (support corrosion), the working electrode potential was cycled between 1 and 1.5 V vs. NHE at a scan rate of 500 mV/s for 10,000 cycles. This protocol aggressively simulated the startup-shutdown transients in an operating PEFC (see Fig. S3 under supporting information). For evaluating the stability of the electrocatalyst (Pt dissolution), the working electrode potential was cycled between 0.6 and 0.95 V vs. NHE for 10,000 cycles to simulate full load-no load transients in an automotive drive cycle (see Fig. S6 under supporting information). Both series of tests were performed in nitrogen-saturated electrolyte at room temperature. The support stability test was also performed on the catalyzed support to investigate the impact of platinum catalyst on the corrosion rate. For each AST, CVs were periodically recorded at regular intervals during the test to monitor the extent of support and/or catalyst degradation. Vulcan XC-72 carbon was used as a baseline catalyst support and 46.5% Pt/C obtained from TKK was used as the baseline electrocatalyst for benchmarking purposes.

2.7. Preparation of MEAs

MEAs were prepared by spraying multiple layers of catalyst ink directly onto both sides of a Nafion® 211 membrane. After both the anode and cathode catalyst layers were applied, the MEAs were hot pressed at 60 °C for 30 s at 2000 psi. All prepared MEAs had an active area of 5 cm². The Pt loading at the cathode, estimated gravimetrically, was 0.4 mg/cm² and the Pt loading at the anode was 0.2 mg/cm². Additional details about ink preparation and MEA preparation are provided under supporting information.

2.8. Performance of MEAs prepared with baseline Pt/C and Pt/TRO electrocatalysts

Polarization curves were obtained using a Compact Fuel Cell Test System model 850C (Scribner Associates, Inc.). The performance testing was conducted at 80 °C with an inlet relative humidity of 75% (corresponding to a saturator dew point of 73 °C). Stoichiometric ratios of 2 for the anode and cathode, with minimum flows of 0.2 SLPM were employed during testing. Further details about operating conditions and oxidants used are provided under supplementary information.

3. Results and discussion

3.1. X-ray diffraction (XRD) measurements

Fig. 1 shows the XRD patterns of TRO-a and TRO-h supports. The main diffraction peaks around 26°, 38.5° and 49° were attributed to the anatase TiO₂ (1 0 1), (0 0 4) and (2 0 0) planes, respectively [48]. No evidence was observed for presence of RuO₂ in the sample dried at 120 °C (TRO-h). As the support was annealed at 450 °C

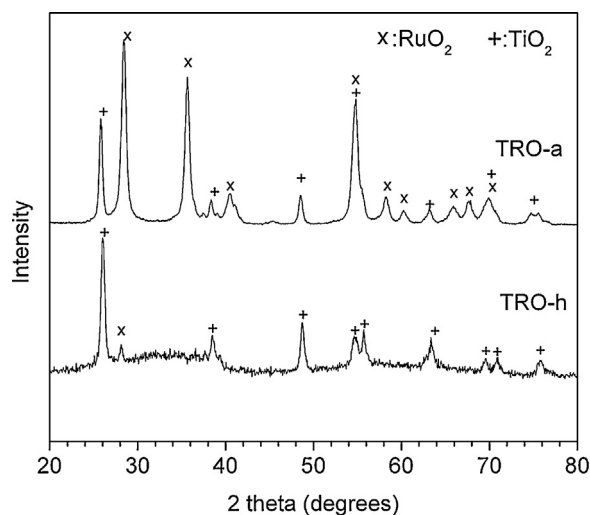


Fig. 1. XRD patterns of TRO-a and TRO-h.

to yield TRO-a, the main diffraction peaks of RuO₂ were observed around 28°, 36° and 55° and were attributed to the rutile (1 1 0), (1 0 1) and (2 1 1) planes, respectively [48]. All new diffraction peaks arising due to annealing could be assigned to RuO₂ and it was concluded that only two distinct phases of anatase TiO₂ and rutile RuO₂ were present in the annealed support (TRO-a). There was no incorporation of Ru inside the TiO₂ crystallite (i.e., no mixed phases).

Fig. 2 shows the XRD patterns of Pt deposited on TRO-a and TRO-h. The main diffraction peaks around 39°, 46° and 68° were attributed to the Pt (1 1 1), (2 0 0) and (2 2 0) planes, respectively [49]. The crystallite size was estimated using the Scherrer equation [50] using the Pt (1 1 1) peak as a reference. The average Pt crystallite sizes for Pt/TRO-a and Pt/TRO-h were 6 and 5.6 nm respectively. Additional heat treatment was conducted at 200 °C and 450 °C. The catalyst obtained was denoted as Pt/TRO-a-*b*, where *b* represents the annealing temperature to which the catalyst was exposed. With heat treatment, the Pt crystallite size increased from 6 nm in Pt/TRO-a to 14 nm in Pt/TRO-a-450, indicating the aggregation of Pt particles, in line with expectations. The diffraction pattern of Pt/TRO-a-200 was identical to that of Pt/TRO-a and hence is not shown in the figure.

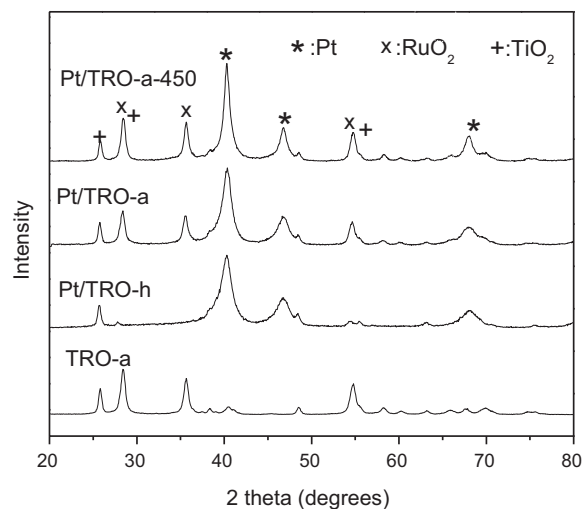


Fig. 2. XRD patterns of Pt/TRO-a-450, Pt/TRO-a, Pt/TRO-h and TRO-a.

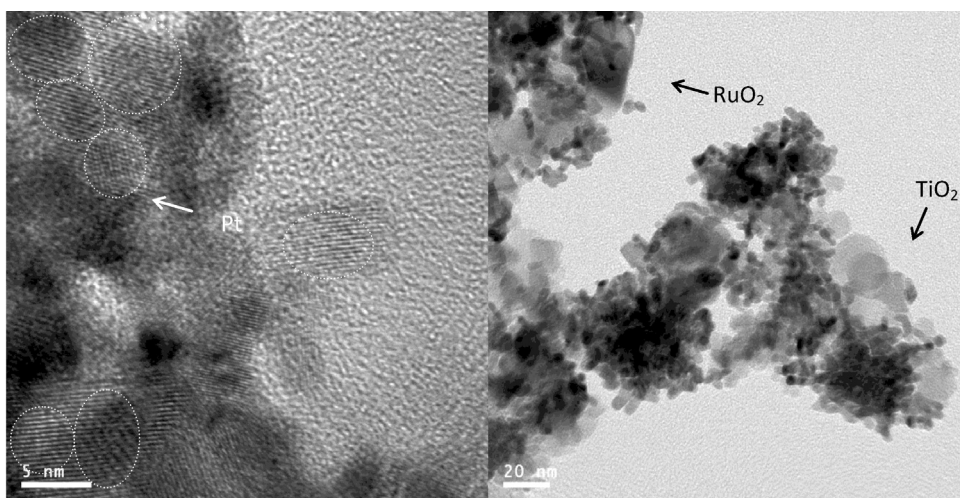


Fig. 3. TEM images of Pt/TRO-a.

3.2. TEM micrographs

TEM micrographs of the Pt/TRO-a catalyst are shown in Fig. 3. Pt nanoparticles were well dispersed on the support surface. Pt nanoparticles were found to be uniformly dispersed within the support material as shown in Fig. S2 and found to be on the surface of both TiO_2 and RuO_2 oxides. Although some of the Pt may be rendered electrically isolated, the close contact between these oxides ensured that the majority of the Pt particles were available for electrochemical activity. The particle size of the Pt nanoparticles was in the range of 4–8 nm, which was consistent with the estimated Pt crystallite size of 6 nm. From the images, it was observed that the RuO_2 exhibited particle-like morphology within the TiO_2 network, instead of forming a film along its surface. EDX analysis and elemental mapping of Pt/TRO-a catalyst confirmed that while there was good dispersion (adequate for percolation and ensuring electrical conductivity), the TiO_2 surface was not completely covered by RuO_2 . Please see Figs. S1 and S2 under supplementary information.

3.3. BET surface area and electrical conductivity

The BET surface area and electrical conductivity of the uncatalyzed and catalyzed supports have been summarized in Table 1. The BET surface area of the TRO materials was lower than that of carbon by a factor of 2–6. The electrical conductivity of all the catalyzed and uncatalyzed supports studied were on the same order as that of Vulcan carbon, confirming that these materials were well suited (in terms of electrical conductivity) for use in PEFC electrodes and for other electrochemical applications. The conductivity value for obtained for the baseline Vulcan carbon sample was found to be consistent with prior values reported in the literature [51–53]. The variations seen in the literature values can be attributed to the fact that electrical conductivity measurements are subject to sample preparation and compression pressure, which were different for each study. Nevertheless, the values obtained in our study lie in the same range as values reported in the literature. The increase in conductivity observed when TRO-h was converted to TRO-a was attributed to the crystallization of the amorphous TRO-h. This crystallization also enhanced particle aggregation, leading to a decrease in BET surface area. A similar trend – enhanced electrical conductivity – was seen when Pt/TRO-a- was further annealed to yield Pt/TRO-a-450.

3.4. Electrochemical characterization

3.4.1. Electrochemical surface area (ECSA) using RDE

The ECSA of Pt/C, Pt/TRO-a, Pt/TRO-a-200, Pt/TRO-a-450 were 52, 32, 32, and 24 m^2/g , respectively. The result agreed well with XRD data. The smaller the crystallite size (particle size), the higher was the ECSA observed. The ECSA of Pt/TRO-h could not be calculated because of the high pseudocapacitive current due to presence of hydrous RuO_2 , which masked the hydrogen adsorption/desorption peaks.

3.4.2. Support stability

The cyclic voltammograms (CVs) recorded for Vulcan XC-72 carbon during the accelerated support stability test (potential cycling between 1 and 1.5 V vs. NHE; 10,000 cycles, see Fig. S3) showed evidence of surface oxide formation through increased peak current assigned to the hydroquinone–quinone (HQ–Q) redox couple of carbon [54] (Fig. S4). In contrast, the shape of CVs for TRO-a remained identical before and after the accelerated support stability test (Fig. S5). The result suggested that the annealed TRO was electrochemically stable and was not further oxidized or reduced after the AST, which agreed with previous reports [55]. The stability of the support was quantified by measuring the change in capacitance (including double layer and pseudo capacitance) calculated at 0.4 V as a function of potential cycling. As seen in Fig. 4(a), this change was only 5%, in the case of TRO-a. This was in sharp contrast with the baseline carbon support, which exhibited a 230% change in capacitance, indicating instability under the test conditions. This support stability tests unequivocally confirmed the high stability of the TRO-a supports under aggressive and relevant test conditions. TRO-h exhibited a change in capacitance of 46% under corresponding conditions. While this was superior to the baseline carbon, the poor ECSA and activity of the Pt/TRO-h electrocatalyst rendered TRO-h unsuitable for PEFC applications.

3.4.3. Catalyst stability

Platinum has been reported to accelerate the rate of carbon support corrosion [56]. The durability of the catalyzed support was evaluated by monitoring the loss in the ECSA of the electrocatalyst as a function of cycle number under the load cycling protocol (potential cycling between 0.6 and 0.95 V vs. NHE, see Fig. S6). The loss of ECSA during this test is caused by Pt dissolution and redeposition or Ostwald ripening and via Pt aggregation [9,10]. The catalyst stability test was not conducted only for catalysts deposited on

Table 1
BET surface area and electrical conductivity of supports and catalysts.

	Vulcan XC-72	TRO-a	TRO-h	46% Pt/C (TKK)	Pt/TRO-a	Pt/TRO-h	Pt/TRO-a-450
BET (m ² /g)	207 ± 4	33 ± 4	97 ± 8	–	–	–	–
Electrical conductivity (S/cm) ^a	31 ± 5	21 ± 5	10 ± 3	26 ± 2	81 ± 7	24 ± 1	69 ± 3

^a Measured at room temperature.

TRO-h because of the relatively lower electrochemical stability of these supports and the poor ECSA of the Pt/TRO-h electrocatalysts.

The TKK Pt/C benchmark catalyst and the Pt/TRO-a catalyst showed a similar reduction of ECSA (~45%) over 10,000 cycles (Fig. 4(b)). This result was in line with expectations—having a more stable support in itself was not expected to minimize the other modes of platinum dissolution and migration that are in play. The stability of Pt/TRO-a could be improved with modest heat treatment. When the Pt/TRO-a catalyst was annealed at 200 °C for 8 h, the loss in ECSA over 10,000 cycles decreased to 35% despite the initial crystallite size and ECSA remaining the same for both samples. When the annealing temperature was further increased to 450 °C, the ECSA of the catalyst decreased due to an increase in platinum particle size during annealing. The loss in ECSA over 10,000 cycles also decreased to about 20%. This apparent increase in stability is due to the lower surface free energy of the larger Pt particles obtained upon annealing [57]. Since a key objective is to improve platinum dispersion and minimize platinum particle size, anything

more than a modest annealing of the catalyzed support (at 200 °C) is unlikely to be practical.

The capacitive current at potentials between 0.4 and 0.6 V due to charging/discharging of the double layer was also recorded during the accelerated load cycling test on the catalyzed supports. The capacitive current remained the same for all tested catalysts (Figs. S7–S10) over 10,000 cycles. The results indicated that the TRO and C supports did not corrode under this AST protocol and confirmed that the loss observed in ECSA was primarily caused by dissolution/aggregation of platinum instead of support corrosion.

The durability of the catalyzed support (Pt/TRO-a) was evaluated under the start-stop AST (Fig. S3) as well, to examine the impact of platinum nanoparticles on the rate of support corrosion. The shape of CVs obtained remained identical before and after the AST (Fig. S11). The result confirmed that TRO was electrochemically stable even upon addition of platinum and that platinum did not catalyze or accelerate the TRO corrosion reaction, unlike in the case of Pt/C [56].

3.4.4. Fuel cell performance and polarization data analysis

The H₂/air performance of MEAs prepared with Pt/TRO-h, Pt/TRO-a, Pt/TRO-a-450 and benchmark 46.5 wt% Pt/C (TKK) are shown in Fig. 5. The polarization data obtained on these MEAs with four different oxidants (O₂, air, helox and 4% O₂) are plotted in Figs. S12–S15 (under supporting information). The polarization results clearly show that Pt/TRO-a has very promising performance in an operating fuel cell comparable to and even exceeding performance obtained using other non-carbon support materials [41,43] under similar operating environments.

The polarization data obtained was analyzed following the method initially proposed by Williams et al. [58] and subsequently utilized by Sambandam et al. [59,60]. The analysis is briefly described here, please refer to Williams et al. [58] for details. The objective of this analysis was to quantitatively estimate key ohmic, mass transport, and kinetic parameters as well as the distribution of overpotentials in the MEAs prepared using

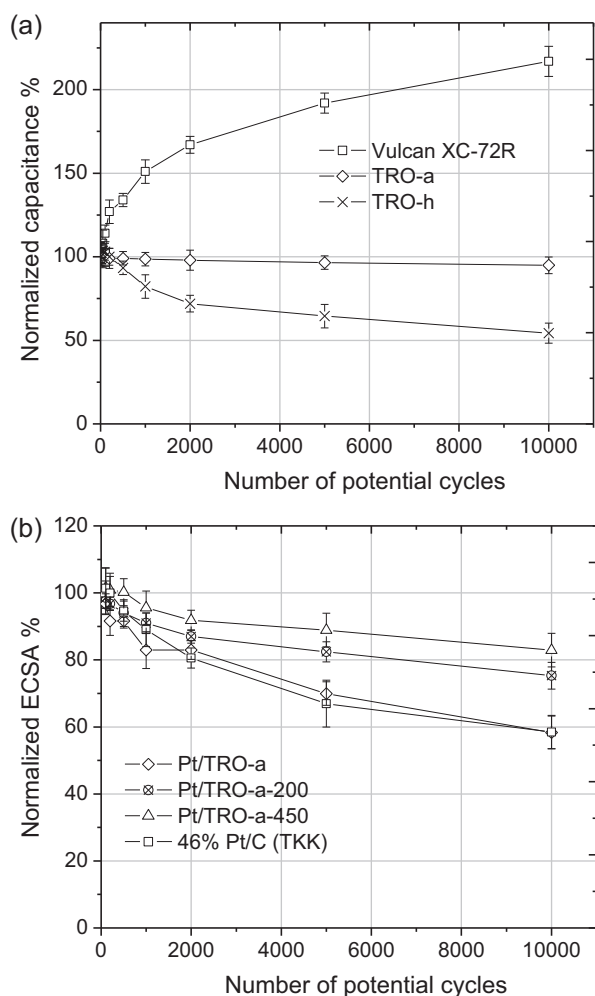


Fig. 4. (a) Change of normalized capacitance of the catalyst supports as a function of cycle number. (b) Loss of ECSA of the catalysts as a function of cycle numbers.

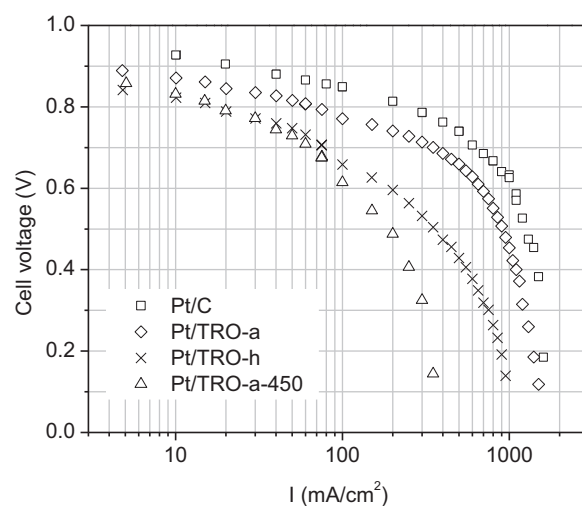


Fig. 5. Polarization data for H₂/air PEFCs with different catalysts at 80 °C, 75% RH and ambient pressure. 2 times stoichiometric flow rate of reactants. Anode catalyst loading: 0.2 mg/cm² and cathode catalyst loading: 0.4 mg/cm².

Table 2Sources of overpotential: H₂/air operation at 80 °C and 75% RH at current densities of 400 mA/cm² and 1000 mA/cm².

Overpotential (mV)	Pt/C		Pt/TRO-a		Pt/TRO-h		Pt/TRO-a-450	
	<i>i</i> = 400	<i>i</i> = 1000	<i>i</i> = 400	<i>i</i> = 1000	<i>i</i> = 400	<i>i</i> = 1000	<i>i</i> = 400	<i>i</i> = 1000
$\eta_{\text{ohmic, non-electrode}}$	23 ± 2	58 ± 5	23 ± 1.2	56 ± 3	24 ± 3	54 ± 7	23 ± 1.7	N/A
$\eta_{\text{ohmic, electrode}}$	13 ± 0.8	32 ± 2	22 ± 1.3	55 ± 3.3	74 ± 3 ^a	185 ± 9 ^a	118 ± 7	N/A
$\eta_{\text{conc, non-electrode}}$	29 ± 1.5	67 ± 3.4	33 ± 2.3	140 ± 8	39 ± 1.6	194 ± 14	324 ± 29	N/A
$\eta_{\text{conc, electrode}}$	0	30 ± 1.2	0	22 ± 0.7	112 ± 8	129 ± 6	127 ± 4	N/A

^a The values reported are approximate since the parameter R_e could not be accurately estimated.

the various electrocatalysts studied. Implementing the methods described, four main sources of polarization losses were estimated: (1) nonelectrode ohmic overpotential ($\eta_{\text{ohmic, non-electrode}}$, due to ohmic losses in the electrolyte membrane and any contact resistances); (2) electrode ohmic overpotential ($\eta_{\text{ohmic, electrode}}$, due to ohmic losses in the electrode); (3) non-electrode concentration overpotential ($\eta_{\text{conc, non-electrode}}$, due to mass transport losses in the GDL and through binder film in the electrode where oxygen is not consumed); and (4) electrode concentration overpotential ($\eta_{\text{conc, electrode}}$, arising from mass transport losses due to combined reaction and diffusion within the electrode where oxygen is consumed).

Ohmic losses: Table 2 reports the overpotential at two different current densities, 400 and 1000 mA/cm², with air as oxidant, for each MEA tested. The non-electrode ohmic overpotential ($\eta_{\text{ohmic, non-electrode}}$) was similar for the MEAs prepared with the TRO based catalysts. Given that all MEAs had the same membrane, in principle, there should have been no variation in membrane resistance. The observed values suggested that the contact resistances at the membrane electrode interface were similar for the Pt/C and the Pt/TRO based electrodes. The effective “electrolyte + contact” resistances are reported in Table 3.

The ohmic resistance in the electrode, R_e , was estimated using the data corrected for $\eta_{\text{ohmic, non-electrode}}$. Under certain assumptions [58], the ratios of current densities of O₂ to air should be equal to 4.76 (ratio of oxygen concentration O₂ and in air) at a fixed overpotential. The polarization data was iteratively adjusted using various R_e values until this condition was satisfied. The calculated R_e values for MEAs prepared using Pt/C and Pt/TRO-a were 33 and 56 mΩ cm², respectively (Table 3). The value obtained for the Pt/C-based electrode was in line with expectations and was largely attributed to the resistance to proton transport in the electrode layer. The higher R_e for TRO-a compared to C (despite its similar or higher conductivity) suggested that in addition to electrical conductivity, the distribution of ionomer within the electrode was important. This is governed by the surface properties and the pore structure of the catalyst support, neither of which were optimized in this study. In the case of Pt/TRO-h and Pt/TRO-a-450, the estimated R_e values were much higher (at 187 and 300 mΩ cm², respectively). These estimates were however not deemed to be very accurate. The difficulty arose because of the substantially poorer performance of MEAs prepared with Pt/TRO-h and Pt/TRO-a-450,

which rendered the iterative method to estimate R_e ineffective. The method employed did not yield precise current ratios in the case of the latter two supports. Accordingly, no conclusions were drawn from the latter two estimates of R_e .

Mass transport losses: To obtain $\eta_{\text{conc, non-electrode}}$, the limiting current density (i_{lim}) was estimated for each MEA. The procedure [58] involves altering the i_{lim} iteratively until the plot of $\log(1/(1 - i/i_{\text{lim}}))$ vs. overpotential yielded a straight line. The final i_{lim} values are reported in Table 3. The $\eta_{\text{conc, non-electrode}}$ was calculated at each current density by finding the difference in voltage between the initial and corrected curves. The $\eta_{\text{conc, non-electrode}}$ was larger for the MEA prepared with Pt/TRO-a, especially at higher current densities. Given that the gas diffusion layers used were the same, this observation was attributed to the fact that the TRO-a support was significantly denser than carbon, which resulted in a much thinner catalyst layer and a lower available catalyst surface for ionomer deposition. Since the ionomer to catalyst ratio was unchanged in all cases, the Pt/TRO based MEA had a much thicker ionomer layer covering the catalyst surface, and hence was more prone to condensed phase transport limitations. Transport of oxygen through this binder film was hindered, leading to larger $\eta_{\text{conc, non-electrode}}$. Amongst the 3 different TRO supports, the magnitude of this overpotential tracked well with the limiting current densities that were estimated by this analysis. The much larger transport losses seen in the case of TRO-h and TRO-a-450 was attributed to water accumulation within the electrode layer (further discussion substantiating this attribution is presented below).

The overpotential due to combined reaction and transport ($\eta_{\text{conc, electrode}}$) in the cathode was estimated by extrapolating the Tafel slope from the activation region and subtracting this “kinetic” Tafel slope line from the overpotential corrected for all ohmic and non-electrode concentration losses. To calculate the kinetic Tafel slope, in mV/dec, the activation-controlled region where current density was 10–100 mA/cm² was used to ensure that concentration overpotentials, ohmic overpotentials, as well as mixed-potentials could be neglected. This overpotential was almost identical for the Pt/C and the Pt/TRO-a based MEAs. The other TRO supports resulted in substantially higher mass transport losses within the electrode.

To identify whether O₂ transport within the various electrodes studied was hindered by gas phase and/or condensed phase diffusion limitations, the helox–air gain was plotted against the O₂–air

Table 3Characteristic parameters for MEAs tested at 80 °C, 75% RH and ambient pressure. 2 times stoichiometric flow rate of reactants. Anode catalyst loading: 0.2 mg/cm² and cathode catalyst loading: 0.4 mg/cm².

	Pt/C	Pt/TRO-a	Pt/TRO-h	Pt/TRO-a-450
<i>b</i> (mV/dec)	62 ± 3	69 ± 3	79 ± 5	78 ± 4
<i>i</i> ₀ (mA/cm ²)	2.93 ± 0.18 × 10 ^{−3}	3.22 ± 0.16 × 10 ^{−3}	2.84 ± 0.20 × 10 ^{−3}	6.39 ± 0.5 × 10 ^{−3}
<i>j</i> _m (mA mg _{Pt} ^{−1})	131 ± 5	54 ± 3	17 ± 1	39 ± 2
<i>j</i> _s (μA cm _{Pt} ^{−2})	238 ± 10	284 ± 17	N/A	300 ± 15
ECSA (m ² /g-Pt)	55 ± 5	19 ± 2	N/A	13 ± 3
Nonelectrode ohmic resistance (mΩ cm ²)	58 ± 5	58 ± 3	61 ± 8	59 ± 4
Electrode ohmic resistance m (Ω cm ²)	33 ± 2	56 ± 3	187 ± 9 ^a	300 ± 17 ^a
Limiting current, air, (mA cm ²)	1604 ± 118	1580 ± 138	1005 ± 110	405 ± 36

^a The values reported are approximate since the parameter R_e could not be accurately estimated.

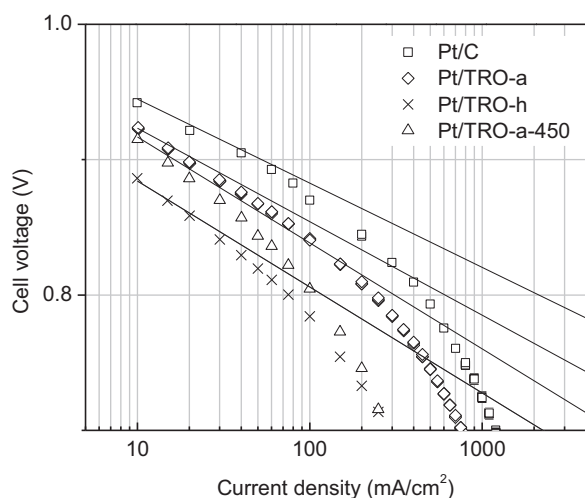


Fig. 6. Analysis of H_2/O_2 polarization data for MEAs with Pt/C, Pt/TRO-a, Pt/TRO-h, and Pt/TRO-a-450. The straight lines correspond to data corrected for ohmic (membrane + cathode) and non-reacting O_2 transport losses.

gain for each current density (Fig. 6) [59]. If there were no mass transfer limitations, the gain plot would reduce down to a cluster of points at (48, 0), corresponding to the expected oxygen-air gain of 48 mV [59]. This is unlikely to be realized in practice. Realistically, the current density at which the points begin to deviate from (48, 0) could be considered as a measure of severity of mass-transport losses. The higher this current density, the less severe the mass transport losses. If gas phase diffusion were a limiting factor, a finite helox-air gain would be observed because O_2 diffusivity in helox is higher than that in air [61]. An oxygen-air gain would also be observed, over and above the expected value of 48 mV [59]. Hence, the gain plot would yield a straight line with a positive slope. On the other hand, if condensed phase diffusion were a limiting factor, the helox-air gain would be close to zero, while the oxygen-air gain would increase, leading to a line with a slope close to zero in the gain plot [59].

By examining the current densities at which the plots departed from (48, 0) [or, alternately, by comparing the position of a fixed current density on the plot], the extent of mass transport losses in the various electrodes was ascertained. The electrode prepared with Pt/C had the lowest mass transport resistance, followed by Pt/TRO-a (almost identical to Pt/C), Pt/TRO-h, and Pt/TRO-450. This trend agreed exactly with findings from the polarization data analysis, reported in Table 3. Both Pt/C and Pt/TRO-a based MEAs exhibited gas phase transport limitations. Among these, Pt/TRO-a showed a greater tendency toward condensed phase transport limitations (smaller slope), which related well to the magnitude of non-reacting transport losses estimated from polarization data analysis (Table 2) and could be attributed to a thicker ionomer film in the Pt/TRO-a electrode (the reason for the thicker ionomer film has been discussed above). In contrast, MEAs based on Pt/TRO-h and Pt/TRO-a-450 both exhibited a clear case of condensed phase transport limitations (evidenced by their near zero slopes). Since the density of these supports were not much different from that of TRO-a, the higher condensed phase transport limitations are attributed to: (1) accumulation of liquid water within the pores of the electrode due to the higher surface hydrophilicity of the TRO-h support. The modest initial slope seen in the case of Pt/TRO-h, followed by its collapse to the abscissa at higher current densities, supports this premise – the rate of generation of water is higher at higher current densities; and (2) the higher platinum particle size (induced by the annealing step) in the case of Pt/TRO-a-450. This in turn leads to lower Pt surface area and a higher effective ionomer

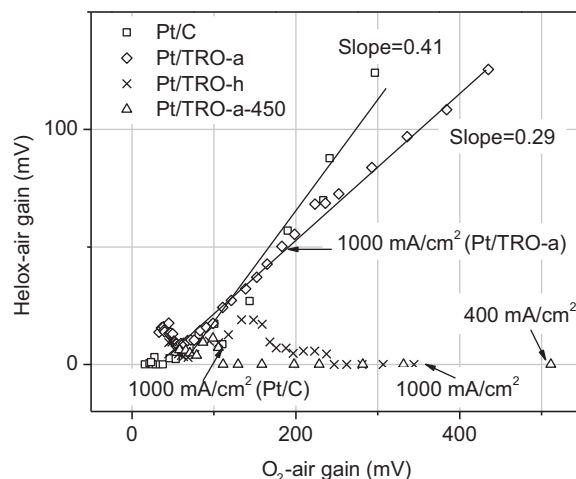


Fig. 7. Helox-air gain vs. O_2 -air gain at 80 °C and 75% RH.

layer thickness surrounding the catalyst particles, and hence higher propensity for condensed phase transport losses.

Activation losses: The H_2/O_2 polarization curves corrected for ohmic and transport losses are plotted in Fig. 7. The Tafel slope, exchange current density (i_0), mass activity ($j_{m, 0.9V, NHE}$), specific activity ($j_{s, 0.9V, NHE}$), and ECSA were calculated and are summarized in Table 3. The results obtained for Pt/C (benchmark) agreed with the literature [62]. The Tafel slopes obtained with Pt/C and Pt/TRO-a catalysts were close to the theoretical value of 70 mV/dec at 80 °C. The larger Tafel slope obtained with Pt/TRO-h and Pt/TRO-a-450 indicated the presence of a mixed activation/transport regime, which was consistent with the finding of water accumulation within the electrode. The Pt/TRO-based catalysts exhibited similar or higher exchange current densities, but lower mass activities than Pt/C, largely due to their larger platinum particle sizes when compared to Pt/C. The specific activities of the Pt/TRO electrocatalysts were similar to or higher than Pt/C, which was due to the low ECSA (platinum utilization) of these catalysts. This suggests that improving the dispersion of platinum on the TRO-a support will substantially improve mass activity and performance.

The performance obtained and the initial mass and specific activities obtained using Pt/TRO-a in this study are promising when taken in conjunction with the exceptional stability of this support toward oxidative degradation and the fact that minimal optimization of the platinum particle size or electrode structure was performed (contrary to the Pt/C electrode, wherein carbon corrosion was severe and optimized and highly refined electrode formulations were used).

4. Conclusions

$\text{TiO}_2\text{-RuO}_2$ (TRO) catalyst supports were synthesized using a wet chemical process. The TRO supports exhibited high electrical conductivity (10–20 S/cm), comparable to baseline Vulcan XC-72 carbon. However, the BET surface areas of the TRO supports were 2–6 times lower than that of carbon. The TRO-a (annealed) support exhibited 10-fold higher electrochemical stability compared to Vulcan carbon when subjected to an aggressive accelerated test protocol that simulated 10,000 start-up and shutdown cycles. Unlike in carbon, the addition of platinum onto the TRO support did not accelerate the support corrosion rate. The particle size of platinum on the surface of TRO support was on the order of 4–8 nm. The fuel cell performance of MEAs prepared using Pt/TRO-a was found to be promising, though slightly lower than that of the Pt/C benchmark. The lower performance was attributed both to the

lower mass activity of the Pt/TRO catalyst (larger Pt particle size) as well as enhanced ohmic and transport losses attributed to the non-optimized nature of the prepared electrodes (in contrast with the optimized Pt/C benchmark). We believe that an effective first step in better optimizing the electrocatalyst layers prepared with Pt/TRO electrocatalysts would be to lower the platinum loading on the support down to about 20%. This will have the twin effect of improving platinum particle size/dispersion, thereby enhancing mass activity, and simultaneously lowering ionomer layer thickness (at current ionomer loading), thereby lowering condensed phase transport limitations. Studies in this direction are ongoing. TRO-h (hydrous) supports were also prepared and interrogated. However, they yielded equivocal stability results and moreover demonstrated very low ECSA and poorer MEA performance due to flooding (and consequently higher transport losses). Similarly, annealed Pt/TRO-a catalysts (Pt/TRO-a-450) also exhibited lower ECSA, poor mass activity, and poor performance. These results were attributed to the larger platinum particle size and the onset of flooding during MEA testing leading to higher mass transport losses. In closing, the outstanding stability of the TRO-a support in conjunction with its excellent electrical conductivity, and the promising activity of electrocatalysts derived from this material renders it an excellent candidate for a corrosion-resistant support, especially for automotive PEFC applications.

Acknowledgements

This work was supported by the US Department of Energy (DOE), Grant # DE-EE0000461. We are also grateful to Dr. Winson C. Kuo, East Asia Application Scientist at Oxford Instrument, and Material Science Service Corp. for their TEM measurement.

Appendix A. Supplementary data

Supplementary data associated with this article can be found, in the online version, at <http://dx.doi.org/10.1016/j.apcatb.2013.03.039>.

References

- [1] W. Vielstich, A. Lamm, H. Gasteiger, *Handbook of Fuel Cells Fundamentals, Technology*, vol. 3, 2003, p. 538.
- [2] E. Antolini, L. Giorgi, A. Pozio, E. Passalacqua, *Journal of Power Sources* 77 (1999) 136.
- [3] M. Uchida, Y. Fukuoka, Y. Sugawara, N. Eda, A. Ohta, *Journal of the Electrochemical Society* 143 (1996) 2245.
- [4] S.C. Thomas, X. Ren, S. Gottesfeld, *Journal of the Electrochemical Society* 146 (1999) 4354.
- [5] Y.Y. Shao, G.P. Yin, Y.Z. Gao, *Journal of Power Sources* 171 (2007) 558–566.
- [6] R. Borup, J. Meyers, B. Pivovar, Y.S. Kim, R. Mukundan, N. Garland, D. Myers, M. Wilson, F. Garzon, D. Wood, P. Zelenay, K. More, K. Stroh, T. Zawodzinski, J. Boncella, J.E. McGrath, M. Inaba, K. Miyatake, M. Hori, K. Ota, Z. Ogumi, S. Miyata, A. Nishikata, Z. Siroma, O. Uchimoto, K. Yasuda, K.-i. Kimijima, N. Iwashita, *Chemical Reviews* 107 (2007) 3904–3951.
- [7] C.A. Reiser, L. Bregoli, T.W. Patterson, J.S. Yi, J.D. Yang, M.L. Perry, T.D. Jarvi, *Electrochemical and Solid State Letters* 8 (2005) A273.
- [8] A. Taniguchi, T. Akita, K. Yasuda, M. Miyazaki, *Journal of Power Sources* 130 (2007) 42.
- [9] P.J. Ferreira, G.J.O. Ia, Y. Shao-Horn, D. Morgan, R. Makharia, S. Kocha, H.A. Gasteiger, *Journal of the Electrochemical Society* 152 (2005) A2256.
- [10] J. Zhang, K. Sasaki, E. Sutter, R.R. Adzic, *Science* 315 (2007) 220.
- [11] D.A. Landsman, F.J. Luczak, *Handbook of Fuel Cells Fundamentals, Technology, and Applications*, 2003.
- [12] G. Wu, Y.S. Chen, B.Q. Xu, *Electrochemistry Communications* 7 (2005) 1237.
- [13] Y.M. Liang, H.M. Zhang, B.L. Yi, Z.H. Zhang, Z.C. Tan, *Carbon* 43 (2005) 3144.
- [14] T. Hyeon, S. Han, Y.E. Sung, K.W. Park, Y.W. Kim, *Angewandte Chemie International Edition* 42 (2003) 4352.
- [15] K.W. Park, Y.E. Sung, S. Han, Y. Yun, T. Hyeon, *Journal of Physical Chemistry B* 108 (2004) 939.
- [16] T. Yoshitake, Y. Shimakawa, S. Kuroshima, H. Kimura, T. Ichihashi, Y. Kubo, D. Kasuya, K. Takahashi, F. Kokai, M. Yudasaka, S. Iijima, *Physica B* 323 (2002) 124.
- [17] C.A. Bessel, K. Laubernds, N.M. Rodriguez, R.T.K. Baker, *Journal of Physical Chemistry B* 105 (2001) 1115.
- [18] F.L. Yuan, H. Ryu, *Journal of Nanotechnology* 15 (2004) S596.
- [19] N. Shang, P. Papakonstantinou, P. Wang, S.R.P. Silva, *Journal of Physical Chemistry C* 114 (2010) 15837–15841.
- [20] S.-E. Jang, H. Kim, *Journal of the American Chemical Society* 132 (2010) 14700–14701.
- [21] A.L. Santos, D. Profeti, P. Olivi, *Electrochimica Acta* 50 (2005) 2615.
- [22] A. Hagemeyer, Z. Hogan, M. Schlichter, B. Smaka, G. Streukens, H. Turner, A. Volpe, J.H. Weinberg, K. Yaccato, *Applied Catalysis A* 217 (2007) 139.
- [23] H. Chhina, S. Campbell, O. Kesler, *Journal of Power Sources* 161 (2006) 893–900.
- [24] X. Cui, J. Shi, H. Chen, L. Zhang, L. Guo, J. Gao, J. Li, *Journal of Physical Chemistry B* 112 (2008) 12024.
- [25] J. Rajeswari, B. Viswanathan, T.K. Varadarajan, *Materials Chemistry and Physics* 106 (2007) 168.
- [26] O.E. Haas, S.T. Briskeby, O.E. Kongstein, M. Tsyppin, R. Tunold, B.T. Borresen, *Journal of New Materials for Electrochemical Systems* 11 (2008) 4.
- [27] G.Y. Chen, S.R. Bare, T.E. Mallouk, *Journal of the Electrochemical Society* 149 (2002) A1092.
- [28] K. Lasch, G. Hayn, L. Jorissen, J. Garche, O. Besenhardt, *Journal of Power Sources* 105 (2002) 305.
- [29] Z. Chen, X. Qiu, B. Lu, S. Zhang, W. Zhu, L. Chen, *Electrochemistry Communications* 7 (2005) 593.
- [30] X. Zhu, H.L.Y. Zhang, Y. Zhang, B. Yia, *Electrochemical and Solid State Letters* 9 (2006) A49.
- [31] B. Seger, A. Kongkanand, K. Vinodgopal, P.V. Kamat, *Journal of Electroanalytical Chemistry* 621 (2008) 198.
- [32] R. Ganesan, J.S. Lee, *Angewandte Chemie International Edition* 44 (2005) 6557.
- [33] M.K. Jeon, H. Daimon, K.R. Lee, A. Nakahara, S.I. Woo, *Electrochemistry Communications* 9 (2007) 2692.
- [34] J.W. Long, R.M. Stroud, K.E. Swider-Lyons, D.R. Rolison, *Journal of Physical Chemistry B* 104 (2000) 9772.
- [35] Q. Lu, B. Yang, L. Zhuang, J. Lu, *Journal of Physical Chemistry B* 109 (2005) 1715.
- [36] L. Jang, G. Sun, S. Sun, J. Liu, S. Tang, H. Li, B. Zhou, Q. Xin, *Electrochimica Acta* 50 (2005) 5384.
- [37] L. Jang, L. Colmenares, Z. Jusys, G.Q. Sun, R.J. Behm, *Electrochimica Acta* 53 (2007) 377.
- [38] K.-W. Park, K.-S. Ahn, Y.-C. Nah, J.-H. Choi, Y.-E. Sung, *Journal of Physical Chemistry B* 107 (2003) 4352.
- [39] S. Trasatti, *Electrochimica Acta* 36 (1991) 225.
- [40] B. Borresen, G. Hagen, R. Tunold, *Electrochimica Acta* 47 (2002) 1819.
- [41] S.-Y. Huang, P. Ganesan, S. Park, B.N. Popov, *Journal of the American Chemical Society* 131 (2009) 13898.
- [42] K.E. Swider, C.I. Merzbacher, P.L. Hagans, D.R. Rolison, *Chemistry of Materials* 9 (1997) 1248–1255.
- [43] V.T.T. Ho, K.C. Pillai, H.-L. Chou, C.-J. Pan, J. Rick, W.-N. Su, B.-J. Hwang, J.-F. Lee, H.-S. Sheu, W.-T.C. Chuang, *Energy & Environmental Science* 4 (2011) 4194.
- [44] J.C. Hicks, C.W. Jones, *Langmuir* 22 (2006) 2676.
- [45] S.H. Sun, D.Q. Yang, D. Villers, G.X. Zhang, E. Sacher, J.P. Dodelet, *Advanced Materials* 20 (2008) 571.
- [46] T.J. Schmidt, H.A. Gasteiger, G.D. Stab, P.M. Urban, D.M. Kolb, R.J. Behm, *Journal of the Electrochemical Society* 145 (1998) 2354.
- [47] T. Han, N.V. Dale, K. Adjemian, V. Nallathambi, S.C. Barton, *ECS Transactions* 41 (2011) 2289–2296.
- [48] J. Zhang, X. Wang, C. Wu, H. Wang, B. Yi, H. Zhang, *Reaction Kinetics and Catalysis Letters* 83 (2004) 229.
- [49] K. Kameyama, S. Shoji, S. Onoue, K. Nishimura, K. Yahikozawa, Y. Takasu, *Journal of the Electrochemical Society* 140 (1993) 1043.
- [50] A. Patterson, *Physical Review* 56 (1939) 978–982.
- [51] M. Uchida, et al., *Journal of the Electrochemical Society* 142 (1995) 2572.
- [52] J. McBreen, et al., *Journal of Applied Electrochemistry* 11 (1981) 787.
- [53] D. Pantea, et al., *Carbon* 39 (2001) 1147.
- [54] K.H. Kangasniemi, D.A. Condit, T.D. Jarvi, *Journal of the Electrochemical Society* 151 (2004) E125.
- [55] C.-C. Hu, Y.-H. Huang, K.-H. Chang, *Journal of Power Sources* 108 (2002) 117–127.
- [56] L.M. Roen, C.H. Paik, T.D. Jarvi, *Electrochemical and Solid State Letters* 7 (2004) A19–A22.
- [57] Y. Sun, L. Zhuang, J. Lu, X. Hong, P. Liu, *Journal of the American Chemical Society* 129 (2007) 15465–15467.
- [58] M.V. Williams, H.R. Kunz, J.M. Fenton, *Journal of the Electrochemical Society* 3 (2005) A635–A644.
- [59] S. Sambandam, V. Ramani, *Electrochimica Acta* 53 (2008) 6328.
- [60] S. Sambandam, V. Ramani, *Physical Chemistry Chemical Physics* 2 (2010) 6140–6149.
- [61] Y.W. Rho, O.A. Velev, S. Srinivasan, *Journal of the Electrochemical Society* 141 (1994) 2084.
- [62] H.A. Gasteiger, S.S. Kocha, B. Sompalli, F.T. Wagner, *Applied Catalysis B: Environmental* 56 (2005) 9–35.